Hydrostatic pressure-induced magnetic and topological phase transitions in the $MnBi_2Te_4$ family of materials

Zhiming Xu,[1] Meng Ye,[1,*] Jiaheng Li,[1] Wenhui Duan,[1,2,3,4,5] and Yong Xu[1,2,3,6,†]

[1]*State Key Laboratory of Low Dimensional Quantum Physics and Department of Physics, Tsinghua University, Beijing 100084, China*
[2]*Tencent Quantum Laboratory, Tencent, Shenzhen, Guangdong 518057, China*
[3]*Frontier Science Center for Quantum Information, Beijing 100084, China*
[4]*Institute for Advanced Study, Tsinghua University, Beijing 100084, China*
[5]*Beijing Academy of Quantum Information Sciences, Beijing 100193, China*
[6]*RIKEN Center for Emergent Matter Science (CEMS), Wako, Saitama 351-0198, Japan*

(Received 23 November 2021; accepted 7 February 2022; published 17 February 2022)

The recent discovery of intrinsic magnetic topological insulator (TI) $MnBi_2Te_4$ has inspired enormous research interest to explore emergent physics created by the interplay of magnetism and topology. Here we systematically investigated the influence of hydrostatic pressure on structural, magnetic, and topological electronic properties of the $MnBi_2Te_4$ family of materials by first-principles calculations. Our results indicate that properties of these layered materials can be effectively tuned by pressure, leading to various kinds of magnetic and topological phase transitions. These include magnetic transitions from *A*-type antiferromagnetism to novel magnetic states, such as frustrated magnetism and intralayer ferromagnetism in conditions of antiferromagnetic intralayer coupling. Moreover, rich topological phase transitions can be driven by pressure in these materials, including trivial insulator to antiferromagnetic TI, type-I or type-II Weyl semimetals, or high-order TI phases. The findings call for in-depth experimental investigations of magnetic and topological physics in these intriguing material systems under high pressure.

DOI: 10.1103/PhysRevB.105.085129

I. INTRODUCTION

Topological materials have attracted enormous research interest in condensed-matter physics because of their unique physical properties and potential applications in electronics, spintronics, quantum computation, etc. [1–3]. Previous research mainly focused on the topological materials whose topological states are protected by time-reversal symmetry (TRS) [4–6]. On the other hand, if the TRS is breaking, intriguing quantum phenomena, such as the quantum anomalous Hall effect and the topological magnetoelectric effect, emerge [7–10]. Therefore, recent research effort has largely been expanded into the study of magnetic topological materials, such as antiferromagnetic (AFM) topological insulators (TIs) [11,12]. To some extent, this is stimulated by the discovery of intrinsic magnetic topological materials, such as the $MnBi_2Te_4$ family of materials [13–16], which provide ideal platforms to explore novel quantum physics induced by the interplay of magnetism and topology [17,17–30]. In addition to the AFM TI state, $MnBi_2Te_4$ can be tuned to other topological phases, such as the magnetic Weyl semimetal (WSM), the chiral Majorana fermion, and the Chern and axion insulators through external magnetic fields or proximity effects [13,17,31]. Similarly, various kinds of magnetic topological states or topological phase transitions can be generated by manipulating magnetic configurations of intrinsic magnetic topological materials, such as $EuCd_2As_2$ [32–35], $EuIn_2As_2$ [36], and EuAgAs [37,38].

Hydrostatic pressure is a conventional and powerful tool to manipulate crystal structures and scales of interactions, which eventually leads to the control of electronic and magnetic properties [39–55]. Through reducing bond length, pressure can enhance the strength of bonding and crystal-field splitting, leading to electronic phase transitions, such as the Bloch-Wilson transition and topological phase transitions [40–46,46]. Pressure can also modify magnetic interactions and drive magnetic phase transitions, such as spin-crossover transitions [48–51], magnetic order transitions [52,53], and spin reorientation transitions [54,54]. Recently high-pressure experiments have been performed to investigate structural, magnetic, and electrical transport properties of the $MnBi_2Te_4$ single crystal [20,21]. However, only a few calculations on pressure/strain-dependent band topology have been carried out [56–58]. Therefore, a comprehensive theoretical study of pressure effects on atomic and magnetic structures of $MnBi_2Te_4$-related materials as well as the associated influence on topological electronic properties is imperative and is the key to interpret experimental results and to further manipulate material properties.

In this paper, based on first-principles density functional theory (DFT) calculations, we systematically investigated the influence of hydrostatic pressure on structural, magnetic, and topological electronic properties of the $MnBi_2Te_4$ family of materials (MnB_2T_4: B = Bi or Sb and T = Te or Se). We predicted a series of magnetic and topological phase transitions

*mengye@mail.tsinghua.edu.cn
†yongxu@mail.tsinghua.edu.cn

in these layered materials due to structural compression under hydrostatic pressure. Magnetic transitions from normal A-type AFM to unusual A-type AFM with intralayer AFM coupling, and finally to geometrically frustrated states are plausible due to enhanced intralayer and interlayer AFM interactions under pressure. Furthermore, variant magnetic topological states, including A-type AFM TI, G-type AFM TI, magnetic type-I or type-II WSM, and high-order TI, can be realized in distinct magnetic phases of these materials under pressure. Our studies shed light on tuning magnetic and topological electronic properties of the $MnBi_2Te_4$ family of materials for fundamental research and device applications.

II. COMPUTATIONAL METHODS

First-principles DFT calculations were performed by the Vienna *ab initio* simulation package [59] using the projector augmented-wave method [60] and the Perdew-Burke-Ernzerhof (PBE) exchange-correlation functional [61]. The generalized gradient approximation (GGA) + U method with $U = 3$ eV in the Dudarev implementation [62] was applied to describe localized d orbitals of Mn atoms, according to previous works [63]. Also a U value of 4 eV was tested for comparison, and its results were summarized in the Supplemental Material [64]. The plane-wave basis with an energy cutoff of 350 eV was employed. The Γ-centered k-point meshes of $18 \times 18 \times 5$ and $18 \times 18 \times 3$ were adopted for self-consistent calculations of ferromagnetic (FM) and A-type AFM phases, respectively. Crystal structures including lattice constants and atomic positions were fully optimized with a force convergence criterion of 0.005 eV/Å. The DFT-D3 method was used to include van der Waals (vdW) corrections [65]. Spin-orbit coupling (SOC) effects were taken into account in the self-consistent calculations. Electronic and topological properties of FM phases were also checked by the modified Becke-Johnson functional methods [66] as performed previously [13]. Tight-binding models based on maximally localized Wannier functions were constructed by the WANNIER90 code [67], and then topological electronic structures were studied by the WANNIERTOOLS package [68].

III. RESULTS AND DISCUSSION

A. Pressure-dependent atomic and magnetic structures

As shown in Fig. 1(a), the tetradymite-type ternary chalcogenides MnB_2T_4 compounds have a layered rhombohedral structure with the space-group $R\bar{3}m$ [69]. The structure can be described by intercalating the Mn-T bilayer into the middle of each B_2T_3 quintuple layer, forming T-B-T-Mn-T-B-T covalently bonded septuple layers (SLs). Different from the strong covalent interactions within the SL, SLs couple weakly with each other through vdW interactions. The optimized lattice constants of $MnBi_2Te_4$ under pressure are shown in Figs. 1(b) and 1(c) where the experimental data [20] are also shown for comparison. As the lattice constants change continuously with pressure, first-order structural transitions do not show up under 15 GPa, which is consistent with the recent high-pressure experiments on $MnBi_2Te_4$ [20,21]. Noticeably, the lattice structure experiences a significant anisotropic compression. At low pressures, the interlayer lattice constant is more sensitive to pressure than the intralayer lattice constant as expected in layered structures. With increasing pressure, the changing rate of intralayer lattice constant a stays almost constant whereas the changing rate of interlayer lattice constant c decreases gradually in our calculations. Overall, the theoretical results are well consistent with experimental ones, showing minor discrepancies (less than 2.3%) in the lattice constant data.

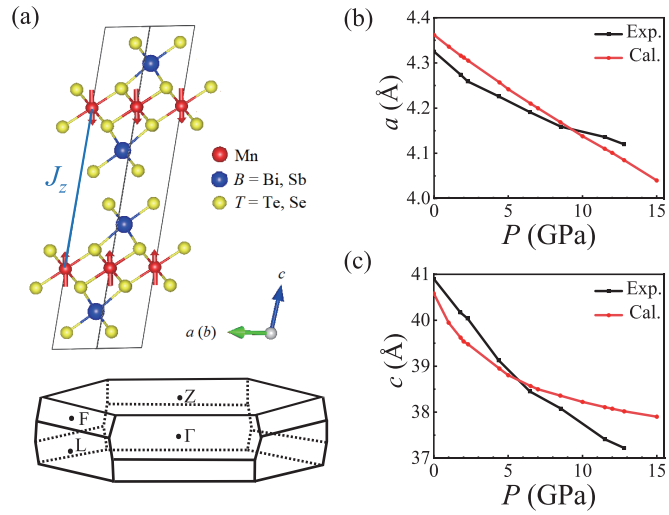

FIG. 1. (a) Crystal structure (top) and Brillouin zone (bottom) of MnB_2T_4 with the A-type AFM ground state. The red, blue, and yellow spheres represent Mn, B, and T, respectively, where B = Bi or Sb and T = Te or Se. Magnetic moments of Mn atoms are denoted by red arrows. The interlayer exchange interaction (J_z) is denoted by the blue line. (b) and (c) Lattice parameters (intralayer lattice constant a and interlayer lattice constant c) of $MnBi_2Te_4$ as a function of pressure. The experimental data are extracted from Ref. [20].

Next we investigated the evolution of magnetic orders of $MnBi_2Te_4$ under pressure. At ambient pressure, the intralayer magnetic coupling is FM, whereas the interlayer magnetic coupling is AFM, forming an A-type AFM magnetic ground state with an out-of-plane easy axis [13]. To determine the magnetic ground state under pressure, we considered eight possible magnetic states with different intralayer and interlayer magnetic configurations. Among them, four intralayer magnetic configurations [Fig. 2(a)], including FM, sAFM, zAFM, nAFM, and two interlayer magnetic configurations (i.e., FM and AFM) were chosen in the calculations. Although each Mn atom has three NNs with equal distance in one neighboring layer due to the threefold rotational symmetry, the interlayer configuration according to our definition only describes the magnetic moments of Mn atoms along the c-axis direction [Fig. 1(a)]. C-type and G-type AFMs are named for intralayer AFM configurations with FM and AFM interlayer configurations, respectively. As we found that variant magnetic structures have negligible influence on the volume in the $MnBi_2Te_4$ family of materials, the enthalpy differences can be replaced by the energy differences.

Energies of different magnetic configurations referenced to the A-type AFM configuration are shown as a function of pressure in Fig. 2(b). The results reveal several important features. First, A-type AFM is energetically favored under

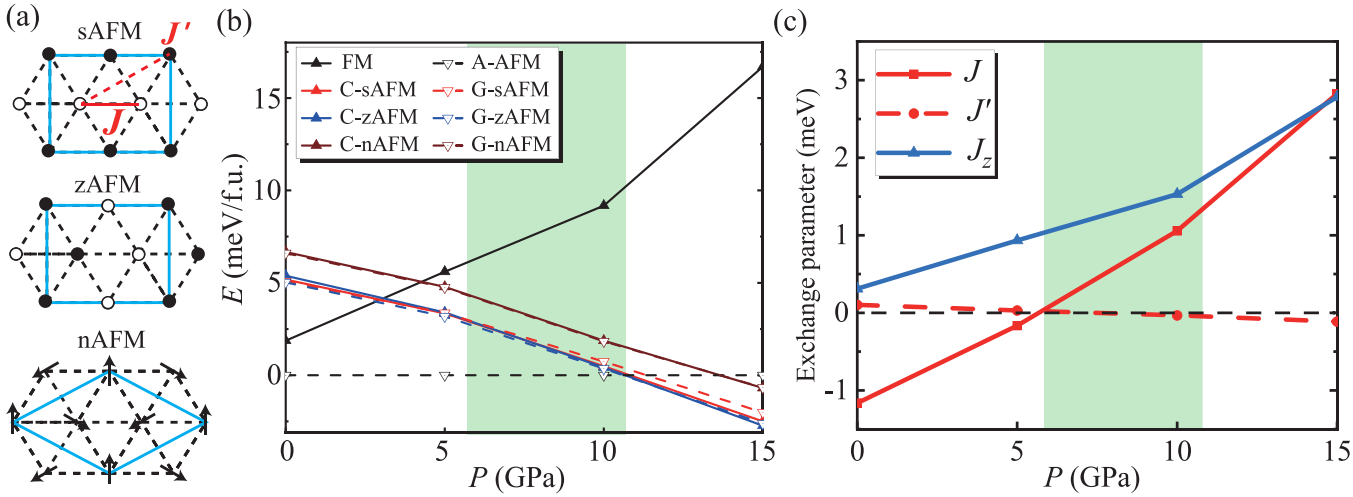

FIG. 2. Evolution of magnetic properties of $MnBi_2Te_4$ under pressure. (a) Three typical intralayer AFM magnetic configurations, including stripy AFM (sAFM), zigzag AFM (zAFM), and noncollinear 120° in-plane AFM (nAFM). Magnetic supercells in DFT energy calculations are denoted by blue lines. Out-of-plane spin-up, out-of-plane spin-down, and in-plane magnetic moments are denoted by solid circles, open circles, and arrows, respectively. The intralayer exchange interactions for nearest-neighbor (NN) (J) and next-nearest-neighbor (NNN) (J') are denoted by red solid and red dashed lines, respectively. (b) Energies of different magnetic configurations as a function of pressure using A-type AFM as a reference. Here, for simplicity, C- and G- refer to C-type AFM and G-type AFM, respectively. For example, C-sAFM refers to the magnetic configuration with intralayer sAFM and C-type interlayer configuration which is an interlayer FM. (c) Exchange coupling parameters as a function of pressure. There emerges an unusual region [illustrated by the light green regions in (b) and (c)] where the intralayer FM configuration is energetically favored even though the intralayer exchange interaction becomes AFM ($J > 0$).

pressures up to 11 GPa. Second, nAFM is, at least, 1.5 meV per formula unit (f.u.) higher in energy than other AFM states. Thus, we will focus on low-energy collinear magnetic states in following discussions. Third, sAFM and zAFM, which share the same exchange interactions between the NNs, display minor energy differences (less than 0.3 meV/f.u.), implying that the exchange coupling between the NNNs is negligible. Fourth, there are tiny energy differences between C- and G-type AFMs, indicating that the total interlayer magnetic interaction is negligible for systems with intralayer AFM configurations. Given that intralayer Mn atoms are crystallized in a trigonal lattice, geometrical frustration would be very likely to occur if the intralayer exchange coupling is AFM under high pressures. This could provide an intriguing material system to investigate frustrated magnetism [70] and its interplay with topological electronic states.

In order to gain an in-depth understanding on the evolution of magnetic interactions under pressure, we constructed an effective Heisenberg spin Hamiltonian,

$$H = \sum_{\langle i,j\rangle_{\text{Intra}}} J\vec{S}_i \cdot \vec{S}_j + \sum_{\langle\langle i,j\rangle\rangle_{\text{Intra}}} J'\vec{S}_i \cdot \vec{S}_j + \sum_{\langle\alpha,\beta\rangle_{\text{Inter}}} J_z\langle\vec{S}_\alpha\rangle \cdot \langle\vec{S}_\beta\rangle,$$

where J, J', and J_z represent the effective exchange coupling parameters for intralayer NN, intralayer NNN, and averaged interlayer coupling, respectively. Here S_i denotes the spin magnetic moment ($5\mu_B$) of the ith Mn atom, which is set to unity in the model Hamiltonian, and $\langle S_\alpha\rangle$ is the averaged spin magnetic moment within the αth layer. For the third term, the value of $\langle S_\alpha\rangle$ equals 1 or -1 for intralayer FM coupling but zero for intralayer AFM coupling, which is consistent with results demonstrated in Fig. 2(b) that the total interlayer coupling is negligible for C-type and G-type AFM states. Therefore, the third term is determined both by the interlayer and by the intralayer magnetic configurations.

The exchange coupling parameters at different pressures were obtained by fitting the energies of different magnetic configurations calculated by DFT, and the results are presented in Fig. 2(c). Obviously, J' is much smaller than other parameters and, thus, can be neglected afterwards. As the pressure increases, both J and J_z become more positive, indicating an enhancement of AFM interactions within and between SLs. Remarkably, J varies from negative to positive at a critical pressure P_{C1} about 6 GPa. Generally, a transition of intralayer magnetic ground state from FM to AFM is expected across P_{C1}. However, the intralayer FM configuration remains energetically favored until about 11 GPa (P_{C2}) even though the intralayer exchange coupling becomes AFM. The region of the unusual intralayer FM state is illustrated by the light green regions in Figs. 2(b) and 2(c), which is rationalized by the competition of J and J_z. For an isolated SL, a positive J prefers intralayer AFM states and even geometrically frustrated states in this triangular lattice. On the other hand, the positive interlayer coupling J_z always prefers the intralayer FM state with an interlayer AFM coupling. Because of the competition between the positive J and the positive J_z, the intralayer FM configuration remains energetically favored above P_{C1}. In the unusual region between P_{C1} and P_{C2}, we expect that its low-energy collective excitations may be interesting, which is subject to further investigations. Eventually, the more rapidly changed J dominates at higher pressure and gives rise to the magnetic phase transition at P_{C2} where A-type AFM becomes energetically unfavored. After the pressure-induced magnetic phase transition, the preferred configuration of the intralayer triangular lattice is AFM, and

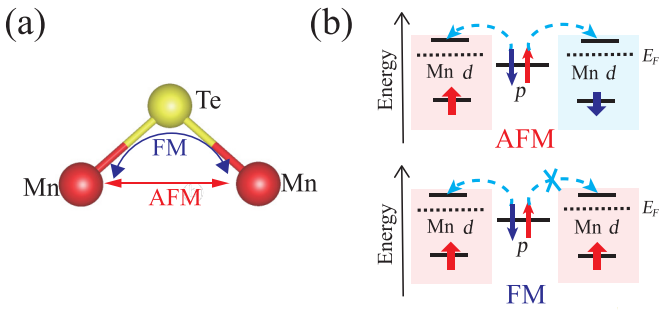

FIG. 3. Schematics of exchange mechanisms. (a) Intralayer magnetic coupling contributed by direct AFM exchange and FM superexchange interactions. (b) Interlayer superexchange interaction mediated by delocalized p orbitals between neighboring magnetic layers for which the AFM configuration is energetically more favorable than the FM one.

the magnetic ground state is highly degenerate, which provides the signature of geometrically frustrated states. In our Supplemental Material [64], we have shown that the tendency of the magnetic phase transition always occurs even at different Hubbard U values (Supplemental Material Fig. S1 [64]). For example, when $U = 4$ eV is chosen, P_{C1} is about 11 GPa, and P_{C2} is above 15 GPa.

Indeed, our theoretical predictions can qualitatively explain the recent transport measurements of $MnBi_2Te_4$ under pressure [20,21]. For example, the resistivity measurements reflect that the Néel temperature (T_N) decreases and finally vanishes with pressure [21], which is consistent with our predicted tendency of the magnetic phase transition from A-type AFM to frustrated magnetic states. Through the Hall resistivity measurement, it is discovered that the spin-flop transition field, which corresponds to the critical magnetic field for the phase transition from A-type AFM to canted AFM, increases with pressure [20] before T_N vanishes. The above observation is in excellent agreement with our finding of enhanced interlayer AFM exchange interaction and out-of-plane magnetic anisotropy (Supplemental Material Fig. S3 [64]) under pressure.

The evolution of intralayer magnetic coupling under pressure can be explained by the competition between the Mn-Mn direct exchange interaction and the Mn-Te-Mn superexchange interaction [63] as shown in Fig. 3(a). In $MnBi_2Te_4$, each Mn atom has a $5\mu_B$ magnetic moment with one spin channel of d orbitals fully occupied and a large spin splitting energy U_d (>7 eV). The direct exchange mechanism favors AFM interaction, and the strength is proportional to t_{dd}^2/U_d, where t_{dd} is the hopping integral between d orbitals. Importantly, the direct interaction is short range and determined by the overlap of neighboring d orbitals, which can be significantly enhanced with decreasing Mn-Mn distances. On the other hand, based on the Goodenough-Kanamori-Anderson rules [71,72], the superexchange interaction through the near-90° Mn-Te-Mn bonds can be FM and is roughly proportional to $-\frac{t_{pd}^4 J_{\mathrm{H}}^p}{4(\Delta_{pd}+U_d)^4}$, where t_{pd}, J_{H}^p, and Δ_{pd} represent the hopping integral between the involved d and p orbitals, the strength of Hund's coupling in ligand p orbitals, and the energy interval between the involved d and p orbitals, respectively [73]. Different from the direct exchange, the Mn-Te-Mn superexchange interaction is not sensitive to the Mn-Mn distances but sensitive to the Mn-Te-Mn bond angle, which determines the magnitude of t_{pd}. According to our calculations, the bond lengths and angles respond differently to hydrostatic pressure. By increasing pressure up to 15 GPa, the Mn-Mn distance decreases by about 7.3%, whereas the near-90° Mn-Te-Mn bond angle changes less than 1°. Therefore, the intralayer direct AFM exchange interaction is greatly strengthened whereas the FM superexchange interaction increases relatively slowly by pressure. Consequently, the effective intralayer exchange interaction J becomes more positive and even favors the AFM interaction under pressure.

The interlayer AFM interaction can be explained by the long-range inter-SL superexchange coupling mediated by delocalized p orbitals between neighboring magnetic layers [24,74]. As shown in Fig. 3(b), doubly occupied p orbitals gain kinetic energy by virtual hopping to unoccupied d orbitals, and the energy gain is more pronounced for interlayer AFM configurations than interlayer FM configurations due to the Pauli exclusion principle. Such a kind of interlayer AFM superexchange is enhanced by pressure which reduces interlayer distances and increases interlayer orbital hybridizations.

As the numerical results are dependent on the choice of U value (Supplemental Material Fig. S1 [64]), we briefly analyze the influence of U. The Hubbard U raises (lowers) the energies of empty (occupied) d orbitals, affects orbital hybridizations, and, therefore, has a significant impact on exchange interactions. A larger U value leads to a larger spin splitting U_d, more localized d electronic states, weaker orbital hybridizations t_{dd}, and weaker direct AFM exchange interactions, which eventually contribute to a less positive J.

We also studied the influence of pressure on atomic and magnetic structures in other $MnBi_2Te_4$ family of materials, which shows similar trends as found in $MnBi_2Te_4$ (see Supplemental Material Fig. S2 [64]). For instance, the lattice structures experience highly anisotropic changes under hydrostatic pressure. Both intralayer and interlayer AFM interactions are enhanced with pressure, and the A-type AFM state remains energetically favored under moderate pressures. Noticeably, the magnetic phase transition occurs in $MnBi_2Se_4$ and $MnSb_2Se_4$ below 15 GPa where G-type AFM is the magnetic ground state (Supplemental Material Figs. S2(e) and S2(f) [64]). Moreover, the magnetization prefers the out-of-plane direction, and the magnetic anisotropy energy [(MAE), the energy difference between out-of-plane and in-plane magnetizations] becomes larger under higher pressure (Supplemental Material Fig. S3 [64]). On the other hand, there are some quantitative differences in magnetic interaction energies, which are attributed to different atomic distances, electronegativities, and SOC strength. For example, the lattice structure shrinks from MnB_2Te_4 to MnB_2Se_4, leading to an increase in intralayer AFM Mn-Mn direct exchange interactions. The electronegativity difference between Mn and Te is smaller than that between Mn and Se, thus, the orbital hybridization between Mn and Te is larger, resulting in stronger interlayer AFM superexchange interaction in MnB_2Te_4 than in MnB_2Se_4 [24]. The SOC strength becomes stronger with heavier elements, leading to the largest MAE in $MnBi_2Te_4$

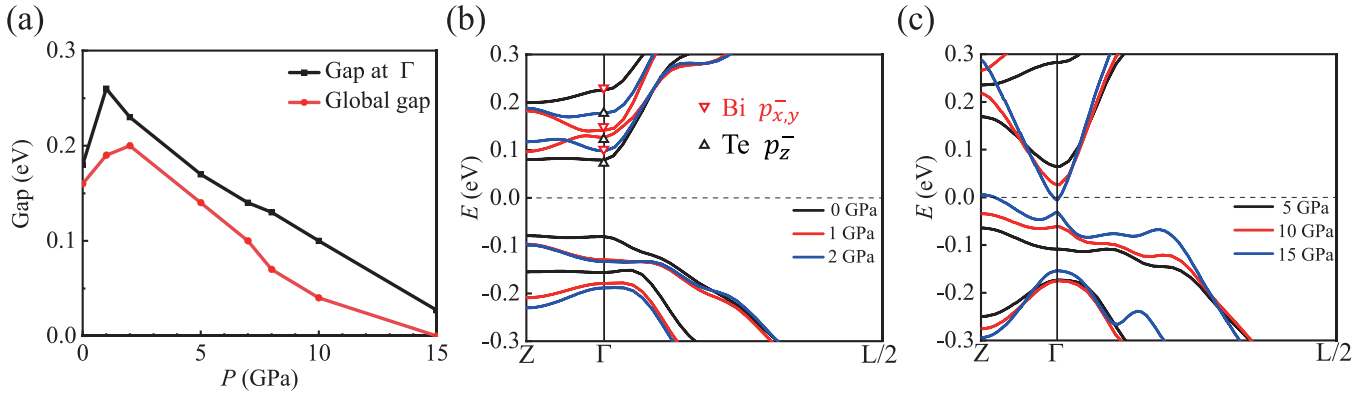

FIG. 4. Influence of hydrostatic pressure on the electronic structure of *A*-type AFM $MnBi_2Te_4$. (a) Direct band gap at Γ and global band gap as a function of pressure. (b) and (c) Evolution of the band structure with pressure (only the band edges are shown). (b) From 0 to 2 GPa, there is a change in band order at the bottom of the conduction bands. Here black upward-pointing and red downward-pointing triangles represent antibonding p_z orbitals of Te and bonding $p_{x,y}$ orbitals of Bi, respectively. "+" and "−" represent parities of Bloch wave functions. (c) The band gap gradually closes from 5 to 15 GPa.

(0.33 meV/f.u.) and the smallest one in $MnSb_2Se_4$ (0.06 meV/f.u.).

B. Pressure-dependent topological electronic structures

We first focus on the evolution of topological electronic structure under pressure for the *A*-type AFM phase of $MnBi_2Te_4$. Under ambient pressure, $MnBi_2Te_4$ is an AFM TI protected by the symmetry $S = \Theta T_{1/2}$, where Θ is TRS and $T_{1/2}$ is the translation of a half lattice constant along the *c* axis [11]. In contrast to time-reversal invariant TIs, the topological surface states of this AFM TI is gapped when the *S* symmetry is broken, for instance, on the top surface. In $MnBi_2Te_4$, bands close to the Fermi level are majorly contributed by the *p* orbitals of Bi and Te, whereas the *d* orbitals of Mn are far away from the Fermi level. Remarkably, the system has an inverted band order at Γ with the p_z^+ orbital of Bi located at the valence-band maximum (VBM) and the p_z^- of Te at the conduction-band minimum (CBM) where the ± sign denotes parity. Similar to Bi_2Te_3, the band inversion induced by the SOC occurs between states of opposite parities, leading to a topologically nontrivial phase.

The electronic structure under pressure is shown for *A*-type AFM $MnBi_2Te_4$ in Fig. 4. The global band gap and direct band gap at Γ both exhibit a nonmonotonic behavior: They first increase at low pressure and then decrease under moderate pressures [Fig. 4(a)]. Focusing on the Γ point, we can divide the evolution into two stages. In the first stage (0–2 GPa) as shown in Fig. 4(b), there is a band order change involving two bands at the bottom of conduction bands (CBs). One band is mainly contributed by antibonding p_z^- orbitals of Te which is the CBM at ambient pressure, and the other consists of the bonding $p_{x,y}^-$ orbitals of Bi. Pressure induces upwards (downwards) shifts of antibonding (bonding) orbitals, resulting in an increase in band gap until about 1 GPa at which the two bands are inverted. In the second stage (2–15 GPa) as shown in Fig. 4(c), band width is broadened under pressure, and a global band gap is reduced until an insulator-metal transition occurs without further topological band inversion between occupied and unoccupied states.

Note that the choice of Hubbard *U* in DFT + *U* calculations does not qualitatively affect the calculated electronic structures near the band edges since the Mn *d* bands are far away from the Fermi energy. However, the predicted band gaps and critical pressures for phase transitions are quantitatively affected. For instance, the predicted global band gaps have a minor difference of less than 10 meV between $U = 3$ and 4 eV. The critical pressure that corresponds to the closure of the global band gap in $MnBi_2Te_4$ is predicted to be 15 GPa at $U = 3$ eV and larger than 15 GPa at $U = 4$ eV.

Although pressure has a minor influence on the band topology of *A*-type AFM $MnBi_2Te_4$, the situation changes in other $MnBi_2Te_4$ family of materials. Compared to $MnBi_2Te_4$, the other family members have weaker SOC and, thus, have topologically trivial band structures at ambient pressure. For these materials, the evolution of band structures under pressure can be divided into three stages as shown in Fig. 5(e). In the first stage, pressure induces a closure and then a reopening of the band gap, leading to a topological phase transition from a trivial insulator to an AFM TI as illustrated by an example study of $MnBi_2Se_4$ in Figs. 5(a)–5(c). The nontrivial band topology of the AFM TI phase is confirmed by calculations of parities of occupied electronic states [4], the evolution of Wannier charge centers, and topological surface states (see the Supplemental Material [64]). The critical pressures of topological phase transitions are predicted to be 0.1, 1.2, and 1.4 GPa for $MnSb_2Te_4$, $MnBi_2Se_4$, and $MnSb_2Se_4$, respectively. Overall, materials with lighter elements require higher pressure to become AFM TIs. In the second and third stages, pressure drives a change in band order at the bottom of CBs and then an insulator-to-metal transition as found in $MnBi_2Te_4$. Under pressure up to 15 GPa, $MnSb_2Te_4$ is predicted to experience these three stages (Supplemental Material Fig. S4 [64]), whereas $MnBi_2Se_4$ and $MnSb_2Se_4$ only experience the first two stages (Figs. 5(a)–5(d), Supplemental Material Fig. S7 [64]).

As discussed in the previous section, pressure can enhance intralayer AFM interactions and, thus, change the magnetic ground state of $MnBi_2Se_4$ from *A*-type to *G*-type AFM above 7 GPa (Supplemental Material Fig. S2(e) [64]). In the *A*-type

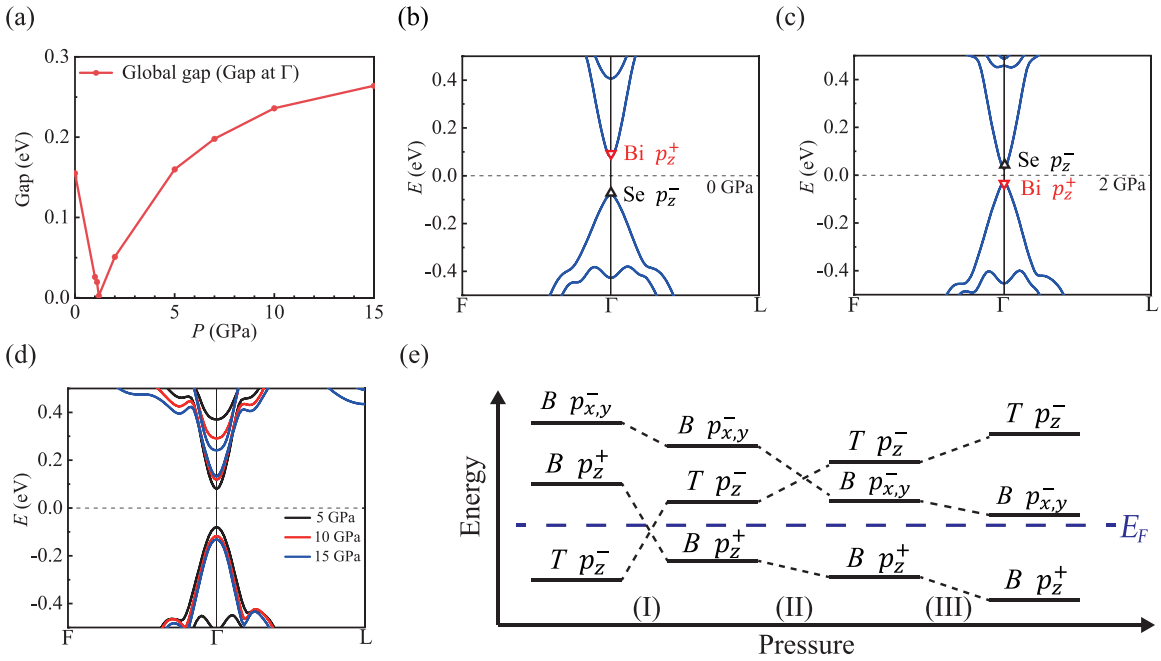

FIG. 5. (a)–(d) Influence of hydrostatic pressure on the electronic structure of *A*-type AFM $MnBi_2Se_4$. (a) The global band gap as a function of pressure. Different from $MnBi_2Te_4$, the global band gap of $MnBi_2Se_4$ is also the direct gap at Γ. (b)–(d) Evolution of the band structure with pressure (only the band edges are shown). From 0 to 2 GPa, pressure induces a band inversion at Γ, leading to a topological phase transition from (b) a trivial insulator to (c) an AFM TI. Here black upward-pointing and red downward-pointing triangles represent antibonding p_z orbitals of Se and bonding p_z orbitals of Bi, respectively. + and − represent parities of Bloch wave functions. (d) From 5 to 15 GPa, the band gap gradually increases before a change in band orders at the bottom of conduction bands. (e) Schematic of orbital evolution at Γ for *A*-type AFM MnB_2T_4 under pressure, which can be divided into three stages: (I) a topological phase transition, (II) a band order change involving two CBs, and (III) an insulator-metal transition. The blue dashed line denotes the position of the Fermi level (E_F).

AFM phase of $MnBi_2Se_4$, the topological surface states on the top surface is gapped as the S symmetry is broken. While in the *G*-type AFM phase, there emerges another topological invariant Z_2 protected by the combination symmetry operator $S' = \Theta T_{1/2}^{ab}$ [75], where $T_{1/2}^{ab}$ is the translation of half the in-plane lattice constant (see Supplemental Material Fig. S9(a) [64]). Thus, gapped surface states on the top surface in the *A*-type AFM configuration become gapless under pressure, given that the S' symmetry is preserved in the *G*-type AFM configuration, which is confirmed by our surface-state calculations (Supplemental Material Fig. S9(c) [64]). Therefore, pressure can simultaneously change magnetic orders, material symmetries, and topological properties, resulting in a gapped-to-gapless transition in the topological surface states.

By applying a magnetic field, the magnetic configuration in the $MnBi_2Te_4$ family of materials can change from the *A*-type AFM to the FM state [23,27]. Thus, we also investigated the evolution of topological electronic structures under pressure for the FM phase. Unlike the *A*-type AFM phase which has doubly degenerate bands protected by the combination symmetry of space inversion P and time-reversal Θ [76], bands of the FM phase are generally nondegenerate. Previous studies on FM $MnBi_2Te_4$ and $MnSb_2Te_4$ indicate that these systems are WSMs [13,56,77,78] with only one pair of Weyl points (WPs) along Γ-Z as protected by the C_{3z} rotation symmetry. Pressure can effectively tune interlayer orbital interactions and is, thus, expected to have a significant influence on topological bands of WSMs.

The evolution of band structures of FM $MnBi_2Te_4$ under pressure is shown in Fig. 6(a). Under pressure up to 2 GPa, the FM phase remains as a type-II WSM with the coexistence of hole and electron pockets at the Fermi level [79]. Here a topological band inversion occurs at Γ between the bonding p_z orbitals of Bi and the antibonding p_z orbitals of Te. As the pressure increases, the WPs move along Γ-Z towards Γ, and finally meet and annihilate at Γ under pressure between 2 and 5 GPa. Meanwhile, another pair of WPs appears between the two lowest CBs. Since the inversion symmetry is preserved, and the direct band gap of FM $MnBi_2Te_4$ is always nonzero under pressures higher than 5 GPa, a Z_4 topological invariant can be defined by summing the parities of occupied bands at inversion invariant crystal momenta [80]. The parity analysis indicates that FM $MnBi_2Te_4$ above 5 GPa corresponds to a FM high-order TI ($Z_4 = 2$), which hosts gapless chiral hinge states [81].

The band structures of FM $MnSb_2Te_4$ show a distinct pressure-dependent behavior as illustrated in Fig. 6(b). Under ambient pressure, FM $MnSb_2Te_4$ is a type-I WSM with a single pair of WPs close to Γ. With increasing pressure, the WPs move away from Γ, and the topological bands get titled, resulting in a quantum phase transition from type-I to type-II WSMs at about 1 GPa. Under a critical pressure of around 5 GPa, the system experiences a topological band inversion at Γ between the bonding $p_{x,y}$ orbitals of Sb and the antibonding p_z orbitals of Te, which is similar to the transition II depicted in Fig. 5(e). As the pressure further increases,

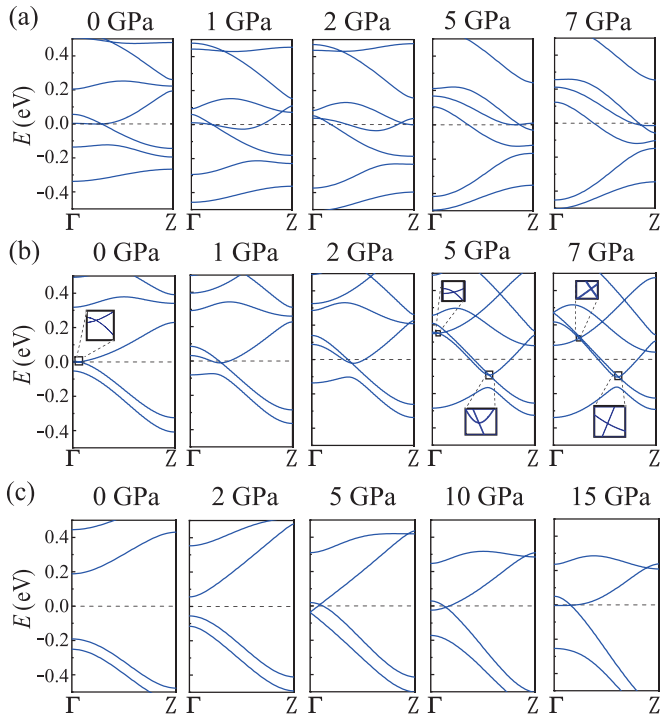

FIG. 6. Band structures of FM (a) $MnBi_2Te_4$, (b) $MnSb_2Te_4$, and (c) $MnBi_2Se_4$ under pressure. Only bands along Γ-Z are shown, which are relevant to the discussion of topological physics.

many additional changes in band orders happen between bands near the Fermi level, giving rise to rich Weyl node structures.

In contrast, FM $MnBi_2Se_4$ and $MnSb_2Se_4$ are trivial insulators under ambient pressure, whose band structures show similar pressure-dependent features as illustrated in Fig. 6(c) and Supplemental Material Fig. S11 [64]. As pressure increases, they sequentially transit from trivial insulators to type-I WSMs at about 5 GPa for $MnBi_2Se_4$ and 7 GPa for $MnSb_2Se_4$, and then to type-II WSMs. To confirm the appearance of WSM phases, we performed surface state calculations for FM $MnBi_2Se_4$ and $MnSb_2Se_4$ at 10 GPa (Supplemental Material Fig. S11 [64]), which clearly show the fingerprint of WSM, i.e., the existence of a Fermi arc connecting the Weyl nodes. Moreover, to see the differences between type-I and type-II WSMs, we performed surface state calculations for FM $MnSb_2Te_4$ at 0.2 and 1 GPa, corresponding to the type-I and type-II phases, respectively (Supplemental Material Fig. S12 [64]). For the type-I phase, there exist a pointlike Fermi surface in the bulk and a Fermi arc linking the two WPs on the side surface. The type-II phase is a little bit different [79]. Therein the bulk Fermi surface include pockets of electrons and holes contacted to each other by Weyl nodes and the Fermi surface of a side surface has intertwined contribution of residual electron and hole pockets linked with a Fermi arc. These systems provide an ideal material platform to study topological and Weyl-related physics.

Considering the vdW correction in DFT is critical to describe the interlayer coupling of the $MnBi_2Te_4$ family of materials and important for predicting materials properties, we systematically checked the influence of vdW correction by performing DFT-PBE calculations without vdW correction and DFT-GGA calculations using different schemes of vdW corrections, including DFT-D3 [65], DFT-TS [82], and vdW density functional optB86b [83,84]. The corresponding results on the atomic, magnetic, electronic, and topological properties of $MnBi_2Te_4$ family of materials are presented in Fig. S13 of the Supplemental Material [64]. The interlayer distances predicted by DFT-D3 and DFT-TS are close to the experimental values, whereas bare PBE (without vdW correction) and optB86b significantly overestimate the interlayer distance (Fig. S13(a) of the Supplemental Material [64]). The overestimation of interlayer distance has minor influence on magnetic properties, leading to a slightly reduced interlayer exchange coupling (Fig. S13(b) of the Supplemental Material [64]). However, this could significantly affect predictions of topological properties when the material structure is near topological phase transition under pressure since the topological band inversion between the delocalized Bp_z and Tp_z depends critically on the strength of interlayer coupling. In bare PBE and optB86b calculations, an extra pressure is demanded to compensate the overestimation in the interlayer distance, thus, usually predicting larger critical pressures of topological phase transition as confirmed for A-type AFM $MnBi_2Te_4$ and $MnBi_2Se_4$ (Fig. S13(c) and S13(d) of the Supplemental Material [64]).

Lastly we discuss temperature effects on electronic properties of the $MnBi_2Te_4$ family of materials, which are closely related to practical applications. Generally, electron-phonon coupling renormalizes electronic band dispersion and meanwhile introduces band broadening (or finite lifetime) for quasiparticles. The effect is negligible at low temperatures but would become increasingly more important at increasing temperature. As extreme examples, previous studies suggest that electron-phonon coupling could drive topological band inversions at high temperatures in topological materials [85–87]. For instance, first-principles calculations show that electron-phonon coupling could change the band gap by about 0.1 eV at 300 K in the Bi_2Se_3 family of materials and, thus, induce topologically nontrivial to trivial phase transitions when the temperature is high enough [87]. Whether electron-phonon coupling could have such significant impact on topological band inversion in the $MnBi_2Te_4$ family of materials remains unknown. Moreover, finite temperature can lead to magnetic phase transitions as well, which, in turn, considerably changes electronic structures and topological properties. Therefore, the profound influence of temperature on properties of magnetic topological materials deserves in-depth investigation in the future.

IV. CONCLUSION

To summarize, we have systematically investigated the influence of hydrostatic pressure on structural, magnetic, and topological electronic properties of the $MnBi_2Te_4$ family of materials. Our results indicate that pressure can effectively tune magnetic orders and induce topological phase transitions. Specifically, we found that both intralayer and interlayer AFM interactions are significantly enhanced by pressure. This could result in rich magnetic phases, such as frustrated magnetic

states and an unusual *A*-type AFM phase where the intralayer exchange coupling has become AFM, but the intralayer FM order can be stabilized by AFM interlayer exchange coupling. Moreover, hydrostatic pressure can effectively tune topological electronic structures, leading to various kinds of electronic phase transitions, including transitions from trivial insulator to AFM TI, AFM TI to metal, trivial insulator to WSM, type-I to type-II WSM, WSM to high-order TI, etc. Our studies present an effective modulation of magnetic and topological electronic properties through hydrostatic pressure and enrich our understanding of magnetism and band topology in magnetic topological materials.

ACKNOWLEDGMENTS

This work was supported by the Basic Science Center Project of NSFC (Grant No. 51788104), the Ministry of Science and Technology of China (Grants No. 2018YFA0307100 and No. 2018YFA0305603), the National Science Fund for Distinguished Young Scholars (Grant No. 12025405), the National Natural Science Foundation of China (Grant No. 11874035), and the Beijing Advanced Innovation Center for Future Chip (ICFC). M.Y. was supported by the Shuimu Tsinghua Scholar Program and the Postdoctoral International Exchange Program.

[1] M. Z. Hasan and C. L. Kane, Rev. Mod. Phys. **82**, 3045 (2010).
[2] X.-L. Qi and S.-C. Zhang, Rev. Mod. Phys. **83**, 1057 (2011).
[3] A. Bansil, H. Lin, and T. Das, Rev. Mod. Phys. **88**, 021004 (2016).
[4] L. Fu and C. L. Kane, Phys. Rev. B **76**, 045302 (2007).
[5] X.-L. Qi, T. L. Hughes, and S.-C. Zhang, Phys. Rev. B **78**, 195424 (2008).
[6] H. Zhang, C.-X. Liu, X.-L. Qi, X. Dai, Z. Fang, and S.-C. Zhang, Nat. Phys. **5**, 438 (2009).
[7] F. D. M. Haldane, Phys. Rev. Lett. **61**, 2015 (1988).
[8] R. Yu, W. Zhang, H.-J. Zhang, S.-C. Zhang, X. Dai, and Z. Fang, Science **329**, 61 (2010).
[9] C.-Z. Chang, J. Zhang, X. Feng, J. Shen, Z. Zhang, M. Guo, K. Li, Y. Ou, P. Wei, L.-L. Wang *et al.*, Science **340**, 167 (2013).
[10] A. M. Essin, J. E. Moore, and D. Vanderbilt, Phys. Rev. Lett. **102**, 146805 (2009).
[11] R. S. K. Mong, A. M. Essin, and J. E. Moore, Phys. Rev. B **81**, 245209 (2010).
[12] C. Fang, M. J. Gilbert, and B. A. Bernevig, Phys. Rev. B **88**, 085406 (2013).
[13] J. Li, Y. Li, S. Du, Z. Wang, B. L. Gu, S. C. Zhang, K. He, W. Duan, and Y. Xu, Sci. Adv. **5**, eaaw5685 (2019).
[14] D. Zhang, M. Shi, T. Zhu, D. Xing, H. Zhang, and J. Wang, Phys. Rev. Lett. **122**, 206401 (2019).
[15] Y. Gong, J. Guo, J. Li, K. Zhu, M. Liao, X. Liu, Q. Zhang, L. Gu, L. Tang, X. Feng *et al.*, Chin. Phys. Lett. **36**, 076801 (2019).
[16] M. M. Otrokov, I. I. Klimovskikh, H. Bentmann, D. Estyunin, A. Zeugner, Z. S. Aliev, S. Gaß, A. Wolter, A. Koroleva, A. M. Shikin *et al.*, Nature (London) **576**, 416 (2019).
[17] Y. Peng and Y. Xu, Phys. Rev. B **99**, 195431 (2019).
[18] Y. J. Chen, L. X. Xu, J. H. Li, Y. W. Li, H. Y. Wang, C. F. Zhang, H. Li, Y. Wu, A. J. Liang, C. Chen, S. W. Jung, C. Cacho, Y. H. Mao, S. Liu, M. X. Wang, Y. F. Guo, Y. Xu, Z. K. Liu, L. X. Yang, and Y. L. Chen, Phys. Rev. X **9**, 041040 (2019).
[19] J.-Q. Yan, S. Okamoto, M. A. McGuire, A. F. May, R. J. McQueeney, and B. C. Sales, Phys. Rev. B **100**, 104409 (2019).
[20] K. Y. Chen, B. S. Wang, J.-Q. Yan, D. S. Parker, J.-S. Zhou, Y. Uwatoko, and J.-G. Cheng, Phys. Rev. Mater. **3**, 094201 (2019).
[21] C. Pei, Y. Xia, J. Wu, Y. Zhao, L. Gao, T. Ying, B. Gao, N. Li, W. Yang, D. Zhang *et al.*, Chin. Phys. Lett. **37**, 66401 (2020).
[22] J. Li, J. Y. Ni, X. Y. Li, H.-J. Koo, M.-H. Whangbo, J. S. Feng, and H. J. Xiang, Phys. Rev. B **101**, 201408(R) (2020).
[23] C. Liu, Y. Wang, H. Li, Y. Wu, Y. Li, J. Li, K. He, Y. Xu, J. Zhang, and Y. Wang, Nature Mater. **19**, 522 (2020).
[24] Z. Li, J. Li, K. He, X. Wan, W. Duan, and Y. Xu, Phys. Rev. B **102**, 081107(R) (2020).
[25] S. Du, P. Tang, J. Li, Z. Lin, Y. Xu, W. Duan, and A. Rubio, Phys. Rev. Res. **2**, 022025(R) (2020).
[26] Y. Deng, Y. Yu, M. Z. Shi, Z. Guo, Z. Xu, J. Wang, X. H. Chen, and Y. Zhang, Science **367**, 895 (2020).
[27] J. Ge, Y. Liu, J. Li, H. Li, T. Luo, Y. Wu, Y. Xu, and J. Wang, Nat. Sci. Rev. **7**, 1280 (2020).
[28] C. Liu, Y. Wang, M. Yang, J. Mao, H. Li, Y. Li, J. Li, H. Zhu, J. Wang, L. Li *et al.*, Nat. Commun. **12**, 4647 (2021).
[29] H.-R. Ji, Y.-Z. Liu, H. Wang, J.-W. Luo, J. Li, H. Li, Y. Wu, Y. Xu, and J. Wang, Chin. Phys. Lett. **38**, 107404 (2021).
[30] J. Ge, Y. Liu, P. Wang, Z. Xu, J. Li, H. Li, Z. Yan, Y. Wu, Y. Xu, and J. Wang, arXiv:2107.03224.
[31] J. Li, C. Wang, Z. Zhang, B.-L. Gu, W. Duan, and Y. Xu, Phys. Rev. B **100**, 121103(R) (2019).
[32] G. Hua, S. Nie, Z. Song, R. Yu, G. Xu, and K. Yao, Phys. Rev. B **98**, 201116(R) (2018).
[33] L.-L. Wang, N. H. Jo, B. Kuthanazhi, Y. Wu, R. J. McQueeney, A. Kaminski, and P. C. Canfield, Phys. Rev. B **99**, 245147 (2019).
[34] J.-Z. Ma, S. Nie, C. Yi, J. Jandke, T. Shang, M.-Y. Yao, M. Naamneh, L. Yan, Y. Sun, A. Chikina *et al.*, Sci. Adv. **5**, eaaw4718 (2019).
[35] J.-R. Soh, F. de Juan, M. G. Vergniory, N. B. M. Schröter, M. C. Rahn, D. Y. Yan, J. Jiang, M. Bristow, P. Reiss, J. N. Blandy, Y. F. Guo, Y. G. Shi, T. K. Kim, A. McCollam, S. H. Simon, Y. Chen, A. I. Coldea, and A. T. Boothroyd, Phys. Rev. B **100**, 201102(R) (2019).
[36] Y. Xu, Z. Song, Z. Wang, H. Weng, and X. Dai, Phys. Rev. Lett. **122**, 256402 (2019).
[37] A. Laha, R. Singha, S. Mardanya, B. Singh, A. Agarwal, P. Mandal, and Z. Hossain, Phys. Rev. B **103**, L241112 (2021).
[38] Y. Jin, X.-T. Zeng, X. Feng, X. Du, W. Wu, X.-L. Sheng, Z.-M. Yu, Z. Zhu, and S. A. Yang, Phys. Rev. B **104**, 165424 (2021).
[39] P. Y. Yu, Phys. Status Solidi B **248**, 1077 (2011).
[40] F. Manjón, R. Vilaplana, O. Gomis, E. Pérez-González, D. Santamaría-Pérez, V. Marín-Borrás, A. Segura, J. González, P. Rodríguez-Hernández, *et al.*, Phys. Status Solidi B **250**, 669 (2013).
[41] I. Efthimiopoulos, C. Buchan, and Y. Wang, Sci. Rep. **6**, 24246 (2016).

[42] W. Ibarra-Hernández, M. J. Verstraete, and J.-Y. Raty, Phys. Rev. B **90**, 245204 (2014).

[43] W. Li, X.-Y. Wei, J.-X. Zhu, C. S. Ting, and Y. Chen, Phys. Rev. B **89**, 035101 (2014).

[44] A. Bera, K. Pal, D. V. S. Muthu, S. Sen, P. Guptasarma, U. V. Waghmare, and A. K. Sood, Phys. Rev. Lett. **110**, 107401 (2013).

[45] M. S. Bahramy, B. J. Yang, R. Arita, and N. Nagaosa, Nat. Commun. **3**, 679 (2012).

[46] P.-L. Gong, D.-Y. Liu, K.-S. Yang, Z.-J. Xiang, X.-H. Chen, Z. Zeng, S.-Q. Shen, and L.-J. Zou, Phys. Rev. B **93**, 195434 (2016).

[47] R. C. Xiao, P. L. Gong, Q. S. Wu, W. J. Lu, M. J. Wei, J. Y. Li, H. Y. Lv, X. Luo, P. Tong, X. B. Zhu, and Y. P. Sun, Phys. Rev. B **96**, 075101 (2017).

[48] R. E. Cohen, I. Mazin, and D. G. Isaak, Science **275**, 654 (1997).

[49] X.-B. Feng and N. M. Harrison, Phys. Rev. B **69**, 035114 (2004).

[50] G. Rollmann, P. Entel, A. Rohrbach, and J. Hafner, Phase Transit. **78**, 251 (2005).

[51] Y. Cheng, X. Wang, J. Zhang, K. Yang, C. Zhang, Z. Zeng, and H. Lin, J. Phys.: Condens. Matter **30**, 155403 (2018).

[52] F. Subhan, I. Khan, and J. Hong, J. Phys.: Condens. Matter **31**, 355001 (2019).

[53] T. Li, S. Jiang, N. Sivadas, Z. Wang, Y. Xu, D. Weber, J. E. Goldberger, K. Watanabe, T. Taniguchi, C. J. Fennie *et al.*, Nature Mater. **18**, 1303 (2019).

[54] J.-Y. Yang, C. Terakura, M. Medarde, J. S. White, D. Sheptyakov, X.-Z. Yan, N.-N. Li, W.-G. Yang, H.-L. Xia, J.-H. Dai, Y.-Y. Yin, Y.-Y. Jiao, J.-G. Cheng, Y.-L. Bu, Q.-F. Zhang, X.-D. Li, C.-Q. Jin, Y. Taguchi, Y. Tokura, and Y.-W. Long, Phys. Rev. B **92**, 195147 (2015).

[55] Z. Lin, M. Lohmann, Z. A. Ali, C. Tang, J. Li, W. Xing, J. Zhong, S. Jia, W. Han, S. Coh, W. Beyermann, and J. Shi, Phys. Rev. Mater. **2**, 051004(R) (2018).

[56] H. Zhang, W. Yang, Y. Wang, and X. Xu, Phys. Rev. B **103**, 094433 (2021).

[57] P. Li, J. Yu, Y. Wang, and W. Luo, Phys. Rev. B **103**, 155118 (2021).

[58] W.-T. Guo, L. Huang, Y. Yang, Z. Huang, and J.-M. Zhang, New J. Phys. **23**, 083030 (2021).

[59] G. Kresse and J. Furthmüller, Phys. Rev. B **54**, 11169 (1996).

[60] P. E. Blöchl, Phys. Rev. B **50**, 17953 (1994).

[61] J. P. Perdew, K. Burke, and M. Ernzerhof, Phys. Rev. Lett. **77**, 3865 (1996).

[62] S. L. Dudarev, G. A. Botton, S. Y. Savrasov, C. J. Humphreys, and A. P. Sutton, Phys. Rev. B **57**, 1505 (1998).

[63] Y. Li, Z. Jiang, J. Li, S. Xu, and W. Duan, Phys. Rev. B **100**, 134438 (2019).

[64] See Supplemental Material at http://link.aps.org/supplemental/10.1103/PhysRevB.105.085129 for more details about the magnetic properties of $MnBi_2Te_4$ calculated with $U = 4$ eV, structural and magnetic properties of other $MnBi_2Te_4$ family of materials, and the influence of hydrostatic pressure on topological electronic properties of the *A*-type AFM, *G*-type AFM, and FM $MnBi_2Te_4$ family of materials.

[65] S. Grimme, J. Antony, S. Ehrlich, and H. Krieg, J. Chem. Phys. **132**, 154104 (2010).

[66] F. Tran and P. Blaha, Phys. Rev. Lett. **102**, 226401 (2009).

[67] G. Pizzi, V. Vitale, R. Arita, S. Blügel, F. Freimuth, G. Géranton, M. Gibertini, D. Gresch, C. Johnson, T. Koretsune *et al.*, J. Phys.: Condens. Matter **32**, 165902 (2020).

[68] Q. Wu, S. Zhang, H. Song, M. Troyer, and A. A. Soluyanov, Comput. Phys. Commun. **224**, 405 (2017).

[69] D. S. Lee, T.-H. Kim, C.-H. Park, C.-Y. Chung, Y. S. Lim, W.-S. Seo, and H.-H. Park, CrystEngComm **15**, 5532 (2013).

[70] L. Balents, Nature (London) **464**, 199 (2010).

[71] J. B. Goodenough, Phys. Rev. **100**, 564 (1955).

[72] J. Kanamori, J. Phys. Chem. Solids **10**, 87 (1959).

[73] J. B. Goodenough, *Magnetism and the Chemical Bond* (Interscience, New York, 1963), Vol. 1.

[74] J. Xiao and B. Yan, 2D Mater. **7**, 045010 (2020).

[75] Y.-J. Hao, P. Liu, Y. Feng, X.-M. Ma, E. F. Schwier, M. Arita, S. Kumar, C. Hu, R. Lu, M. Zeng, Y. Wang, Z. Hao, H.-Y. Sun, K. Zhang, J. Mei, N. Ni, L. Wu, K. Shimada, C. Chen, Q. Liu, and C. Liu, Phys. Rev. X **9**, 041038 (2019).

[76] P. Tang, Q. Zhou, G. Xu, and S.-C. Zhang, Nat. Phys. **12**, 1100 (2016).

[77] T. Murakami, Y. Nambu, T. Koretsune, G. Xiangyu, T. Yamamoto, C. M. Brown, and H. Kageyama, Phys. Rev. B **100**, 195103 (2019).

[78] L. Zhou, Z. Tan, D. Yan, Z. Fang, Y. Shi, and H. Weng, Phys. Rev. B **102**, 085114 (2020).

[79] A. A. Soluyanov, D. Gresch, Z. Wang, Q. Wu, M. Troyer, X. Dai, and B. A. Bernevig, Nature (London) **527**, 495 (2015).

[80] A. M. Turner, Y. Zhang, R. S. K. Mong, and A. Vishwanath, Phys. Rev. B **85**, 165120 (2012).

[81] R.-X. Zhang, F. Wu, and S. Das Sarma, Phys. Rev. Lett. **124**, 136407 (2020).

[82] A. Tkatchenko and M. Scheffler, Phys. Rev. Lett. **102**, 073005 (2009).

[83] J. Klimeš, D. R. Bowler, and A. Michaelides, J. Phys.: Condens. Matter **22**, 022201 (2009).

[84] J. c. v. Klimeš, D. R. Bowler, and A. Michaelides, Phys. Rev. B **83**, 195131 (2011).

[85] I. Garate, Phys. Rev. Lett. **110**, 046402 (2013).

[86] K. Saha and I. Garate, Phys. Rev. B **89**, 205103 (2014).

[87] B. Monserrat and D. Vanderbilt, Phys. Rev. Lett. **117**, 226801 (2016).